ACS NANO
Cite This: ACS Nano XXXX, XXX, XXX–XXX
www.acsnano.org

ARTICLE

Laser-Induced Graphene Composites as Multifunctional Surfaces

Duy Xuan Luong,[†,‡,▽] Kaichun Yang,[§,▽] Jongwon Yoon,[†,∥,▽] Swatantra P. Singh,[⊥,&] Tuo Wang,[†] Christopher J. Arnusch,[*,⊥] and James M. Tour[*,†,#,⊗]

[†]Department of Chemistry, Rice University, Houston, Texas 77005, United States
[‡]Applied Physics Program, Rice University, Houston, Texas 77005, United States
[§]Department of Civil and Environmental Engineering, Rice University, Houston, Texas 77005, United States
[∥]Jeonju Center, Korea Basic Science Institute (KBSI), Jeonju, 54907, Republic of Korea
[⊥]Department of Desalination and Water Treatment, Zuckerberg Institute for Water Research, The Jacob Blaustein Institutes for Desert Research, Ben-Gurion University of the Negev, Sede-Boqer Campus, Midreshet Ben Gurion 84990, Israel
[#]Department of Material Science and NanoEngineering Rice University, Houston, Texas 77005, United States
[⊗]Smalley-Curl Institute and the NanoCarbon Center, Rice University, Houston, Texas 77005, United States

Supporting Information

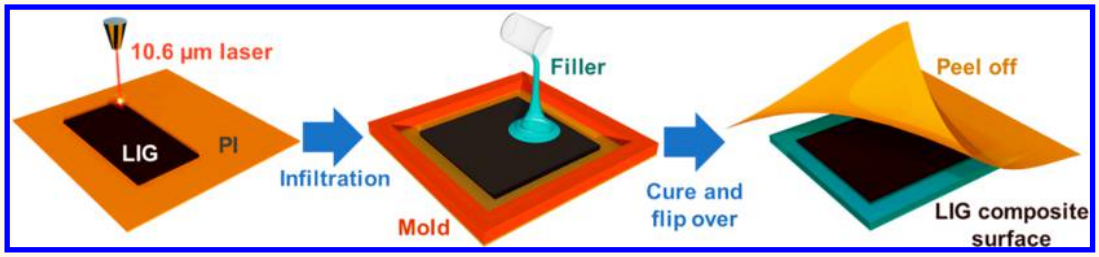

ABSTRACT: **Laser-induced graphene (LIG) is a platform material for numerous applications. Despite its ease in synthesis, LIG's potential for use in some applications is limited by its robustness on substrates. Here, using a simple infiltration method, we develop LIG composites (LIGCs) with physical properties that are engineered on various substrate materials. The physical properties include surface properties such as superhydrophobicity and antibiofouling; the LIGCs are useful in antibacterial applications and Joule-heating applications and as resistive memory device substrates.**

KEYWORDS: *laser-induced graphene, nanocomposite, superhydrophobic, Joule heating, deicing, thermal therapy, memory device, antibiofouling*

Graphene, a two-dimensional carbon nanomaterial that has diverse properties including good electrical conductivity and mechanical strength, is a possible material for a variety of applications in energy storage and flexible electronic and electrochemical catalysis.[1−5] However, realistic applications of the composite are limited by the complex synthesis of graphene that requires high temperature or multiple chemical processes.[6] Recently, a graphenic nanomaterial called laser-induced graphene (LIG) has been widely investigated for a number of applications due to its easy and scalable synthesis.[7−12] LIG is a porous graphene material originally produced through a one-step laser treatment of commercial polyimide (PI) film under an ambient atmosphere.[13] Its physical properties can be controlled by varying experimental conditions including the laser pulse parameters and lasing atmosphere.[14,15] Applications of LIG for energy storage, electrocatalysis, thermal conduction, and water treatment[16−19] have been demonstrated, including exceptional resistance to biofilm growth in water purification applications.[20,21] LIG has evolved into a platform material upon which numerous commercial applications can be envisioned.[22] However, the weak adherence of LIG to the PI substrate hinders its use in some technology applications.[9,21,23]

Previous studies of polydimethylsiloxane (PDMS)/LIG composites have shown potential applications in soft electronics for strain sensors and supercapacitors.[24−27] In this work, which differs from previous studies that focused on PDMS/LIG composites for electronics applications, a one-step infiltration process is developed that enables the transfer of LIG onto a variety of commercial materials from polymers to submicron-sized particles, producing composites for multifunctional

Received: December 20, 2018
Accepted: February 7, 2019
Published: February 7, 2019

DOI: 10.1021/acsnano.8b09626
ACS Nano XXXX, XXX, XXX–XXX

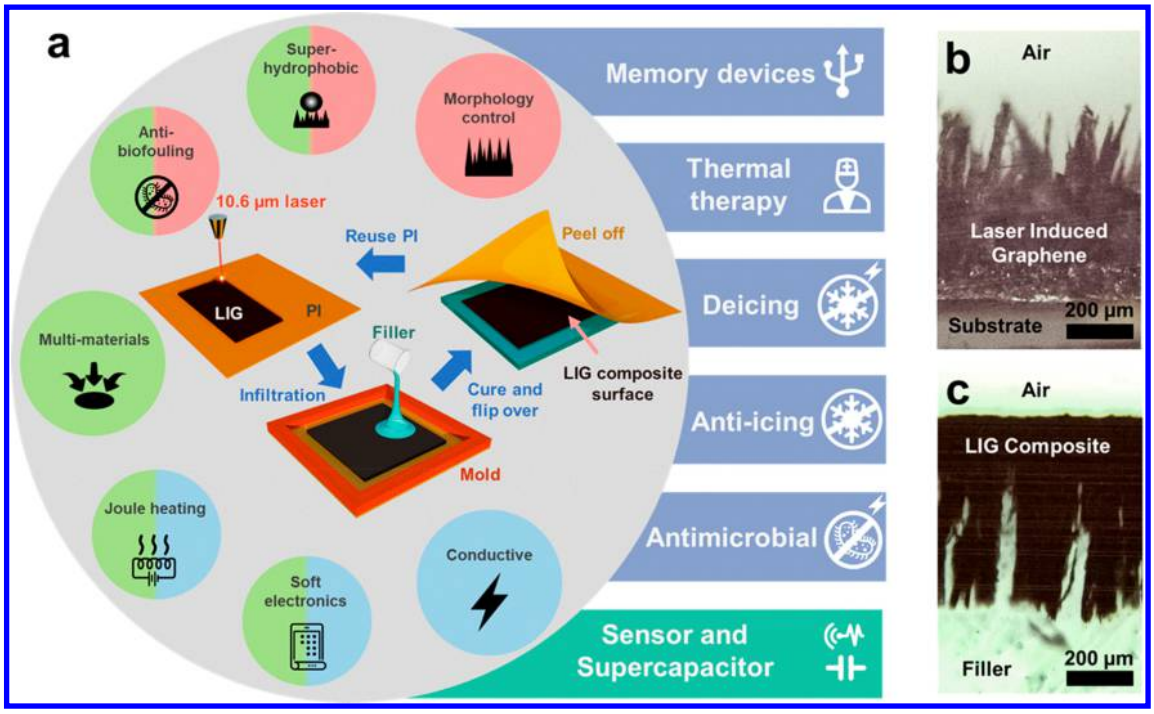

Figure 1. Fabrication process of LIGCs. (a) Schematic of the fabrication of LIGCs. The resultant LIGCs possess multifunctional properties and potential applications that are discussed in this paper. Other applications in soft electronics are strain sensors and supercapacitors.[10,24−26] (b) Optical image of the original LIG fibers (LIGF). The bottom of the LIGF is LIG. (c) Optical image of LIGC−PDMS. Because the LIGC−PDMS is turned upside down and the unreacted PI peeled away, the bottom of the as-made LIG ends up as the surface composite that contacts air. The LIGF becomes part of the bulk composite and forms a high surface area interface with any one of several filler materials.

applications with increased robustness (Figure 1a). This LIG composite (LIGC) has many interesting properties, most derived from the surface morphology and conductivity of the various LIGCs that are potentially useful for multiple applications, as will be discussed.

RESULTS AND DISCUSSION

To fabricate the LIGC, filler materials are infiltrated into the freshly made porous LIG on PI by gravity or through hot pressing into a polymer sheet (Figure 1a and Figure S1). The final cured or solidified product is flipped upside down, and the PI layer is peeled off to reveal the composite surface. LIG forms composites with a wide variety of common materials including solid hydrocarbons, elastomers, epoxy, cement, and geopolymer (Figure S2). In particular, construction materials such as latex paint (LP), Portland cement (PC), and alkaline activated geopolymer (AAG), along with commercial plastics such as polyethylene (PE), polypropylene (PP), and polystyrene (PS), successfully form composites with LIG. The infiltration process is improved with each material to maximize the amount of LIG transferred to the composite (Experimental Section). In previous studies, we discussed two LIG morphologies: the original LIG sheet structure and LIG fiber (LIGF).[14] The laser parameters to produce each form are discussed in the Experimental Section. In LIGF, the fibers form a dense forest on top of LIG that is backed by unreacted PI. By optical microscope and SEM (Figure 1b,c and Figure S3a), LIG forms a high surface area interface with polymers or hydrocarbons such as PDMS, wax, epoxy, and poly(methyl methacrylate) (PMMA) that were liquids, before the infiltration, with few subsequent voids in the composite (Figure S3). In these cases, an entire LIG layer is transferred to the composite (Figure 1b,c and Figure S4). In composites with suspensions or slurry precursor materials such as PC, AAG, or LP, the porosity increases from the bulk outward to the surface of the composite. These composites include LIGC−LP, LIGC−AAG, and LIGC−PC that have the bottom LIG layer partly transferred (Figure S3); this partial transfer results in the rough composite surface of both LIG and LIGF. LIGC−PDMS and LIGC−PC were selected as being representative of liquid and slurry composites for X-ray photoelectronic spectroscopy (XPS) characterization (Figure S5). The surface of the LIGC−PDMS has ∼11% LIG content, while the LIGC−PC composite has ∼61% LIG content at the surface; the liquid PDMS more easily fills the pores of the LIG than does the PC slurry. In Raman spectroscopy, LIG has the expected characteristic features: the D peak at ∼1350 cm^{-1} induced by defects and bending; the G peak at ∼1580 cm^{-1}, and the 2D peak at ∼2700 cm^{-1} from second-order zone-boundary phonons.[28] These features remain in the LIGC with relatively similar D/G and 2D/G ratios (Figure S6), indicating the preservation of the graphene structure in the composites. Introduction of filler to make LIGC stabilizes the flaky surface of LIG. In Figure S7, the surface of LIG is visibly altered even with small mechanical contact. However, the LIGCs are better in terms of visible abrasion resistance and are stable to Scotch-tape tests.

It is known that atmospheric oxygen oxidizes the edge of LIG so that it becomes superhydrophilic.[15] In contrast, when formed under an inert atmosphere such as argon or nitrogen, the LIG becomes superhydrophobic with a contact angle >150°. In LIGF, the base LIG is hydrophobic with a contact angle of 118° but not superhydrophobic because it is somewhat protected from oxygen by the fibrous forest.[14] When hydrophobic materials such as PDMS, wax, PE, PP, or PS are infiltrated into the LIGF and the PI layer is removed, the low oxygen content LIG is brought to the surface. This LIGC now becomes

DOI: 10.1021/acsnano.8b09626
ACS Nano XXXX, XXX, XXX−XXX

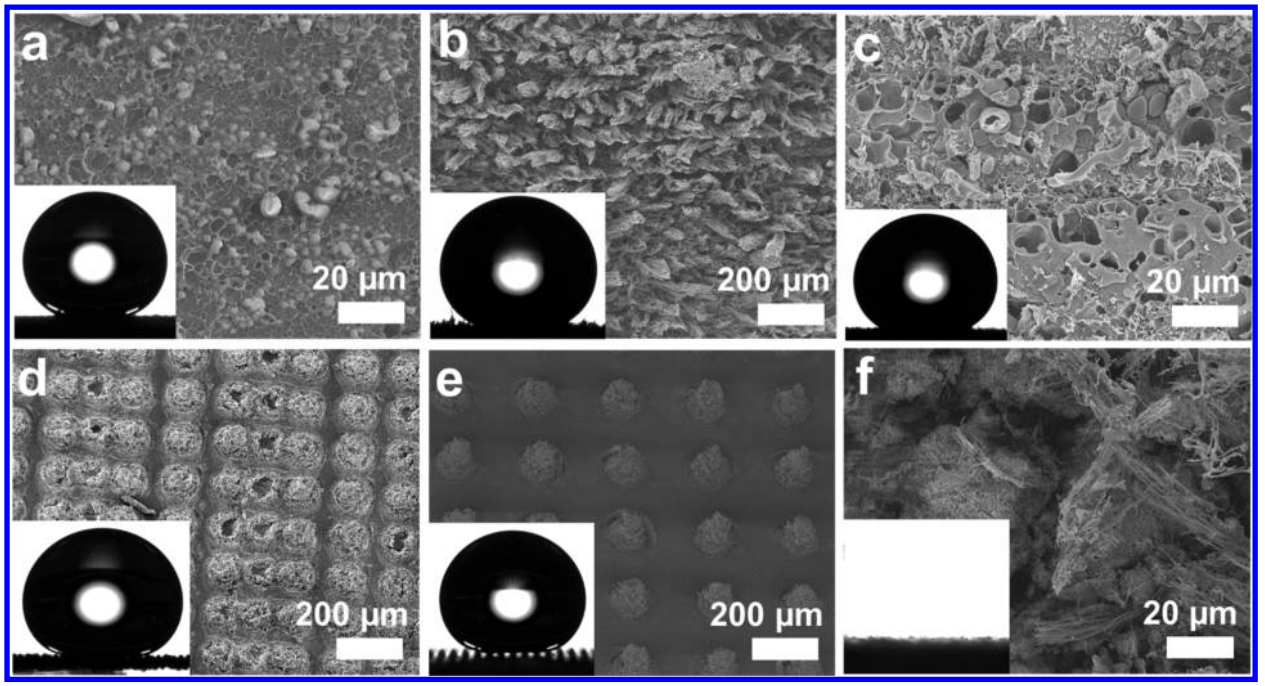

Figure 2. LIGC surfaces and their wetting. SEM images of a LIGC surface and water droplet profiles on these surfaces in the inset. (a) LIGC−PDMS in 500 PPI LIGF with contact angle of 158°. (b) LIGC−PE in 500 PPI LIGF with contact angle of 153°. (c) LIGC−PP in 500 PPI LIGF with contact angle of 151°. (d) LIGC−PDMS in 200 PPI LIGF with contact angle of 161°. (e) LIGC−PDMS in 100 PPI LIGF with a contact angle of 160°. (f) LIGC−PC with contact angle of 0°.

superhydrophobic with a contact angle of >150° (Figure 2a and Figure S8). By scanning electron microscopy (SEM), the LIGC−PDMS composite surface is composed of 11% PDMS (Figure 2 and Figure S9) and has grooves and valleys imprinted from the LIGF (Figure 2a and Figure S9a). This roughness imprinted from the LIGF is hierarchical from micrometer to nanometer scale, changing the LIGFC−PDMS composite from hydrophobic to superhydrophobic.

To further increase the hydrophobicity of the composites, the LIGC is imprinted from the lasing process patterning. We have reported the morphology change from LIG to LIGF by changing the laser pulse density.[14] As the pulse density increases, the laser pulses overlap, etching the top LIGF to form LIG. Decreasing the pulse density results in the preservation of the LIGF, resulting in a thick LIGF forest. In the pulse width modulation laser system, LIG and LIGF are synthesized using pulse densities of 1000 and 500 pulses per inch (PPI, a standard commercial laser setting, 1 in. = 2.54 cm) (Experimental Section), respectively. While LIGC−PDMS from LIGF made at 500 PPI is superhydrophobic, reducing the pulse density further increases the superhydrophobicity. At 200 PPI, the LIGC−PDMS−200PPI results in grooves and valleys formed by the laser pulses. As a result, the hydrophobicity is maximized to a contact angle of 160.8°. Further reducing the pulse density to 100 PPI causes discrete holes throughout the LIG on the PI substrate; this forms upward pointing needles of LIGC−PDMS−100PPI from the bottom of the PDMS (Figure 2). The top of the needles supports the weight of the water droplet that separates it from the base with a contact angle of 160.2°. However, the hydrophobicity of this LIGC−PDMS-100PPI structure is reduced when water reaches the PDMS on the bottom either through condensation or pressure. In this case, wetting transforms the surface from a Cassie−Baxter model to a Wenzel's model (Figure 2 and Figure S9).[29,30]

At the other extreme, LIGC−PC and LIGC−AAG are hydrophilic with a contact angle of 0°. To make the LIGC, LIGF is treated with UV ozone for 2 min to oxidize the edge and make it hydrophilic, facilitating the infiltration of PC and AAG into the LIGF. The resulting LIGCs have porous surfaces (Figure 2 and Figure S9) that quickly wick water droplets inside the composite (video S1).

LIG transferred from the PI substrate to the LIGC retains its low sheet resistance (Figure S10). The level of infiltration is reflected in the surface conductivity. As expected, the LIGC−PDMS, LIGC−epoxy, LIGC−PMMA, and LIGC−wax, with all of the LIG transferred to the composite, show low sheet resistance down to 20 Ω sq^{-1}, similar to that of the original LIG and LIGF. These surfaces have smooth microstructures as seen in Figure S9a. Other composites such as LIGC−LP, LIGC−PP, LIGC−PS, LIGC−PE, LIGC−AAG, and LIGC−PC, with partial LIG transfer, have higher resistance. These surfaces have rough microstructures with visible LIGF bundles on the surface (Figure S9b−i). Previous studies found that LIG composite resistance changes with applied stress.[10,24] The LIGC gauge factor (GF), measured as piezoresistive sensitivity $=\frac{\Delta R/R}{\Delta L/L}$, is tunable by varying the laser pulse density (Figure S11). Interestingly, as the pulse density increases, the surface conductivity and GF increase (Figure S11). GF > 1000 can be obtained at only 5% strain in LIGC−PDMS. This high conductivity of the LIGC composites may have applications in flexible electronic and Joule heating devices.

Graphene-based materials have been exploited as Joule heating devices in construction deicing, domestic heating, and thermal injury therapy by virtue of their high electrical conductivity, ultralight weight, and thermal stability.[31−33] LIGC composite heaters possess outstanding heating efficiency with heating rates up to 2.5 °C s^{-1}. LIGC−LP and LIGC−PDMS are chosen to study the heating process as shown in

DOI: 10.1021/acsnano.8b09626
ACS Nano XXXX, XXX, XXX−XXX

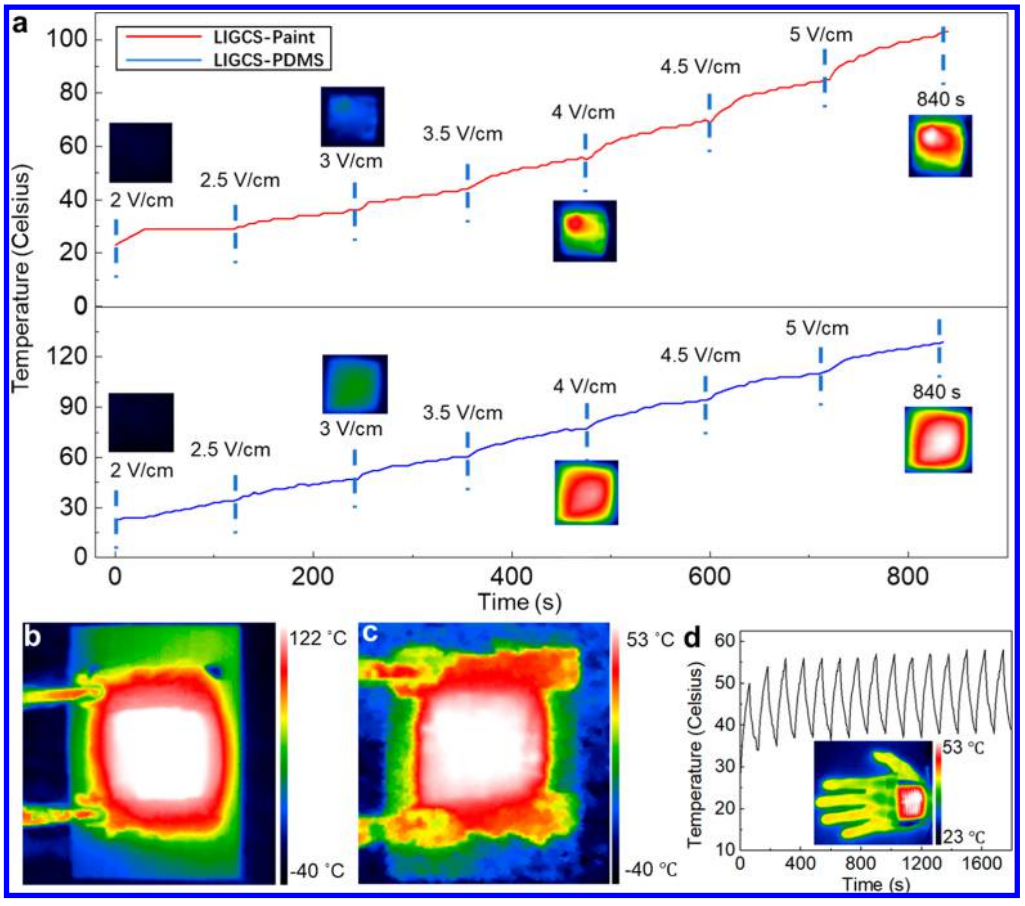

Figure 3. Joule heating applications for LIGC. (a) The temperature increase of LIGC−LP and LIGC−PDMS under stepwise-increased power inputs from 2 V cm^{-1} to 5 V cm^{-1}. The IR photo insets demonstrate saturated temperatures at the end of plateaus under certain power inputs. (b) Infrared (IR) picture of LIGC−LP under 7.5 V cm^{-1} DC bias with maximum temperature 122 °C and background temperature −40 °C. (c) IR picture of LIGC−PC under 7.5 V cm^{-1} DC bias with maximum temperature 53 °C and background temperature −40 °C. (d) Cyclic heating test of LIGC−PDMS thin film as a wearable heater. The IR photo inset shows the comparison of heater, hand, and background temperature.

Figure 3a. By applying constant DC bias at the two ends and increasing it by 0.5 V cm^{-1} every 2 min, the temperature increases linearly then reaches equilibrium, indicating fast heating and stable performance of the device. This linear rate of temperature increase is proportional to the applied power (Figure S12).

LIGC−LP has a high heating rate of 2.5 °C s^{-1} while LIGC−AAG and LIGC−PC heating rates are 0.95 and 0.3 °C s^{-1} with 7.5 V cm^{-1} voltage input (Figure S13). Figure 3b,c shows the IR images of LIGC−LP and LIGC−PC under a dry ice refrigerated environment. The maximum surface temperatures of heated LIGC−LP and LIGC−PC are 122 and 53 °C, well above the freezing point of water in the dry ice environmental with temperature ∼−78.5 °C. LIGC−LP, LIGC−epoxy, LIGC−PP, LIGC−PS, LIGC−PE, and LIGC−PDMS have better LIG infiltration due to their being liquids when they are applied. They wet LIGF without breaking the fibers, thus resulting in higher conductivity. Deicing at an environmental temperature ∼−40 °C was achieved using these LIGCs, with ice sliding off the surface after a DC bias was applied (video S2). Additionally, the superhydrophobic surfaces of LIGC−Wax, LIGC−PDMS, LIGC−PP, LIGC−PE and LIGC−PS prevent incoming droplets from freezing on the surface at −20 °C (video S3). Some of these composites could serve as active deicing surfaces in construction.

LIGC−PDMS thin films can be used as thermal therapy films for body injuries, especially joint and muscle injuries; heating patches are a popular physiotherapy.[27,34,35] As shown in Figure 3d, the stability of the device is tested by a cyclic heating test at a 2.5 V cm^{-1} fixed power input. The IR image of the stretchable heater on a hand demonstrates the temperature comparison during the heating−cooling cycles. In Figure 3a, the plateau of every step underscores the reliable heating performance. In addition, the heater in Figure 3d was stretched up to 60% while maintaining the DC bias (6 V) and the temperature was captured by IR camera in real time, as shown in Figure S14a. The temperature decreased abruptly at first under 20% strain then stabilized. This LIGC−PDMS demonstrates stable heating as the temperature is relatively unchanged for 24 h (Figure S14b).

Resistive random-access memory (RRAM) has been considered as potential nonvolatile memory due to its advantages such as fast write/erase speed, low operation voltage, low power consumption, and good scalability when compared to conventional flash memory.[36,37] RRAM has a simple metal−insulator−metal (MIM) configuration, which has an active material sandwiched between two electrodes. Here, we explore the potential of a LIGC in soft electronics as one component in RRAM. Figure 4a shows a schematic diagram and a photograph of the fabricated LIGC−PDMS−1000PPI memory device. The detailed device fabrication process and a magnified photograph of the fabricated device are described in the Experimental

DOI: 10.1021/acsnano.8b09626
ACS Nano XXXX, XXX, XXX−XXX

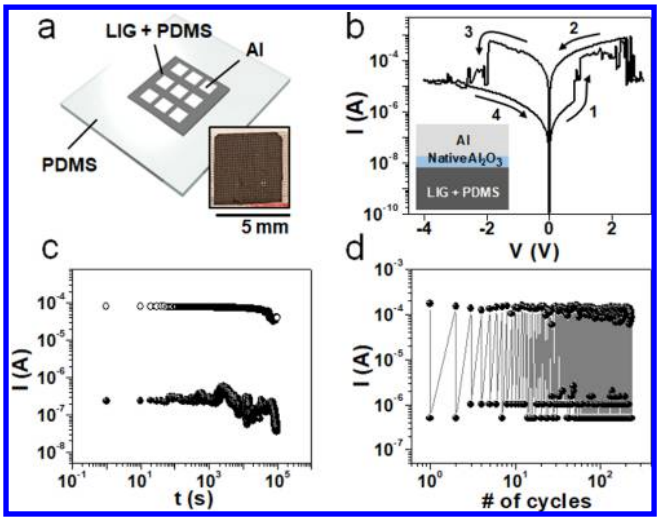

Figure 4. Resistive memory device based on LIGC−PDMS−1000PPI. (a) Schematic diagram and photograph of the fabricated device. (b) Resistive switching characteristics of the fabricated memory device. The inset shows the cross-sectional schematic diagram of the memory device. (c, d) Retention and endurance characteristics of the device.

Section and Figure S15. The fabricated memory device displays a typical bipolar resistive switching characteristic as shown in Figure 4b. The current abruptly increases at +0.8 V (SET) and decreases at −2 V (RESET) with a current ON and OFF ratio (I_{ON}/I_{OFF}) of 10^2−10^3. Interestingly, after O_2 plasma treatment on the surface of the composite, the operational voltage is sharply reduced (Figure S16). This might result because of the smoother surface and higher oxygen content after O_2 plasma treatment, according to SEM, atomic force microscopy (AFM), and XPS analyses (Figures S17−19 and Table S1). O_2 plasma treatment for ∼1 min enhances the electrical properties of the device. The devices treated by O_2 plasma for 3 and 5 min experience significant electrical property degradation as shown in Figure S20 due to surface damage, producing poor electrical contact between the LIGC−PDMS−1000PPI and electrodes. The data retention and endurance characteristics are tested as shown in Figure 4c,d. The current ON and OFF states are well maintained for 10^5 s and 200 SET/RESET cycles with an I_{ON}/I_{OFF} ratio of 10^2−10^3. In the endurance test, the pulse width in SET/RESET operations is 1 ms and amplitude was 2 and −4 V, respectively, at a read voltage of 0.1 V. Furthermore, we conduct a stretching test of the device by applying tensile strain from 0 to 11.5% (Figure S21). The device demonstrates resistive switching behavior up to a tensile strain of 7.7%, with degradation in the electrical properties to some degree; it is not operational at a tensile strain of 11.5% (Figures S22 and S23). The results suggest the potential of using the LIGC−PDMS composite as a stretchable nonvolatile memory device. Carbon and Al contact can induce the resistive switching characteristics by a redox reaction at the interface between carbon and Al, producing native Al_2O_3, which is a known material for resistive switching.[36] The positive bias might result in the local conducting path from oxygen vacancies generated by carbon with strong affinity to oxygen, and the negative bias might annihilate oxygen vacancies due to the oxidation by oxygen in atmosphere (Figure S24). Size-independent switching characteristics of the memory devices suggest that the resistive switching can be induced by a local conducting path (Figure S25).[37−39]

Previously, we reported the exceptional resistance to biofilm formation on LIG made from PI and polysulfone polymers.[20,21,23] However, the LIG derived from PI and polysulfone polymers is relatively brittle, a property that might restrict its use in applications where a robust surface that can resist physical damage is required.[9,23] The susceptibility for biofilm formation on LIGC composites containing construction materials is tested, and it is observed that LIGC−PC, LIGC−AAG, and LIGC−LP are more resistant to biofilm growth compared to the material without LIG (Figure 5). However, for LIGC−PDMS, no benefit is observed (Figure S26). We observe similarly thick biofilm including live and dead bacteria and extracellular polymeric substances (EPS) on the PDMS, LIGC−PDMS, and other filler materials (Figure S27−31). The LIGC−PC, LIGC−AAG, and LIGC−LP surfaces have antifouling effects and show almost no biofilm growth on the surfaces for the duration of the experiment. Possible explanations for this phenomenon can be the surface texture of the LIGCs (Figures S29−S31). The inhibitory effects due to the surface texture of LIGC are observed similarly to the previously reported PI LIG and polysulfone polymer LIG, where rough surfaces were shown to

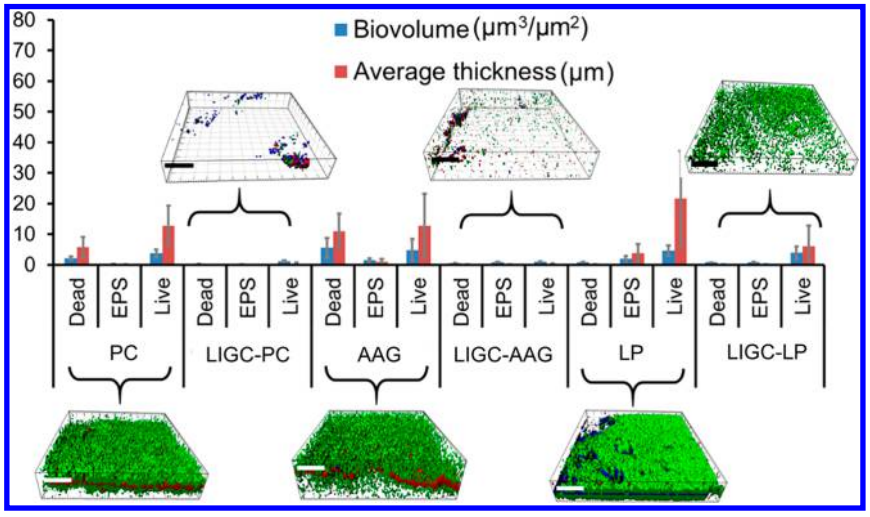

Figure 5. Biofilm growth on different LIGC. Representative IMARIS software images (green and red represents live and dead bacteria, respectively, and blue represents EPS) of PC, LIGC−PC, AAG, LIGC−AAG, LP, and LIGC−LP.

DOI: 10.1021/acsnano.8b09626
ACS Nano XXXX, XXX, XXX−XXX

enhance biofilm resistance.[20] The texture of the LIG within the LIGC−PDMS is masked by the PDMS material surfaces, which might have led to higher biofilm growth in LIGC−PDMS (Figures S27−S28). To visualize the bacterial growth on the surfaces, three-dimensional images of the biofilm are constructed with IMARIS-Bitplane software and represent the averaged quantitative values of biofilm observed for the respective surfaces (Figure 5 and Figure S26). LIGC−PDMS is configured as an electrode to evaluate the antibacterial properties. LIGC−PDMS surfaces show 6 log bacterial reduction in 6 h at 2.5 V; approximately 4 log and ∼2 log bacterial removal is seen at 2.0 and 1.5 V, respectively (Figure S32), whereas at 0 V, no bacterial inhibition is seen. Used as a Joule heater in air there would be a strong surface electrothermal effect for surface antibacterial activity since it can quickly go to high temperatures (Figure 3), for example, if bacteria in the air or dust settles on the surface. If the device in the present configuration is placed in water, due to the high heat capacity of water, there might only be minimal temperature increases and thus no electrothermal antibacterial effect. If compared to the antibacterial assay as we show, an electrode configuration is used and the Joule heating occurs in the water between electrodes, then using the maximum voltage from the antibacterial killing assay of 2.5 V, and an estimated current of 0.1 A, the amount of power available to heat the water is very small. The mechanism is likely the same as previously published.[20,21]

CONCLUSION

We demonstrate a compatible and robust composite with LIG integrated into a variety of materials. Many of the LIGC composites have enhanced hydrophobicity due to specific surface roughness. This roughness is engineered by tuning the laser to optimize the surface characteristics that lead to superhydrophobicity. With high electrical conductivity, LIGCs have potential for use in soft electronics, including wearable thermal therapy and RRAM devices, and in deicing, anti-icing, antibiofouling and antimicrobial applications. This approach offers a series of multifunctional composites that integrate the properties of LIG, producing robust nanomaterials that have applications in multiple fields.

EXPERIMENTAL SECTION

Fabrication of Laser-Induced Graphene. Laser induction is conducted on PI film substrates using a 75 W 10.6 μm CO_2 in Universal Laser System's XLS10MWH platform operating in pulse width modulation. The pulse separation (or image density) varies from 25 to 250 μm (or 1000−100 PPI); the laser scanning speed is fixed at 15 cm s^{-1}. Laser average power is changed by tuning the duty cycle. Most of the experiments are conducted at a fixed 500 PPI at 12% duty cycle. Therefore, when denoted LIGC−XYZ, the LIG is fabricated at that laser parameter.

Infiltration of LIG for LIGC. *LIGC−PC.* PC is from commercial all-purpose QUIKRETE concrete. Before mixing, the concrete mixture is sieved with 100 mesh screens to remove the rocky aggregate; PC is the major remaining component. DI water and PC are mixed together at a ratio of 1:2 and stirred for 5 min to mix the PC slurry or paste. LIG is first UV ozone treated (Boekel 135500) for 5 min to make it hydrophilic. Then it is placed in a plastic mold and wetted by DI water. The PC slurry is poured on top of the LIG in the mold and the mixture is vibrated by hand to remove air and facilitate infiltration of the PC. The mold containing the LIG−PC composite is placed in a plastic box with some water on the bottom of the box to provide a humid environment for curing of the PC. The box is placed on a hot plate at 90 °C for 12 h. The PI film is then peeled away, and the LIGC−PC composite is removed from the mold.

LIGC−AAG. Water glass solution ($Na_2Si_3O_7$ 37% from SCIENCE Co., 18 g) is added to sodium hydroxide (1.23 g, ACS). Then 5 g of the resulting solution is evaporated at room temperature with magnetic stirring. The water glass solution is stirred continuously with a magnetic stirrer to homogeneity and then mixed with metakaolin (10 g, from BASF). LIGF is first UV ozone treated for 5 min to make it hydrophilic then placed in a plastic mold and wetted by DI water. AAG paste is poured on top of the LIGF in the mold and is vibrated by hand to remove air from the LIGF and render a well-infiltrated matrix. The mold containing LIGF and AAG is placed in a plastic dish covered by a lid. Then the dish is placed on a hot plate at 90 °C for 12 h to cure the AAG in a closed plastic box. The PI film is peeled away, and the LIGFCS−AAG is removed from the mold.

LIGC−PDMS. PDMS is made from Sylgard 184 purchased from Dow Corning. The PDMS agents A and B are mixed at a ratio of 1:1 and poured on top of LIGF in a mold. The mold containing the PDMS and LIG is placed under vacuum in a desiccator to remove air. Then it is placed on a hot plate at 90 °C for 12 h to cure the PDMS. The PI film is peeled away, and the LIGC−PDMS composite is removed from the mold.

LIGC−LP. Commercial LP ProMar 200 is purchased from Sherwin-Williams. LIG is first UV ozone treated for 5 min to make it hydrophilic then placed in a plastic mold. LP is first diluted with DI water in 1:1 ratio, and the solution is used to wet the LIG. After this initial infiltration, the sample is dried on a hot plate at 90 °C. Then the undiluted paint is poured to fill the entire mold. After drying at 90 °C for 3 days, the PI film is removed.

LIGC−Epoxy. A two-part commercial epoxy (Hardman General Purpose Epoxy) is mixed and poured on top of the LIG. After curing, the PI film is removed.

LIGC−Wax. Commercial wax is melted and poured on top of the LIG. After solidification, the PI film is removed.

LIGC−PMMA. 950 PMMA A4 is poured on top of the LIG. After drying at 90 °C and curing at 120 °C, the PI film is removed.

Hot Pressing of LIG for LIGC. *LIGC−PE, −PP, and −PS.* Thermoplastic materials including PE, PP, and PS are used to fabricate LIGC using a hot-pressing process. Slices of the plastic and LIGF are stacked between two glass slides with pressing from both sides. The entire setup is placed on a hot plate at 170 °C, and a 1 kg weight is placed on the top glass slide to press LIG fiber into the partially melted plastic.

Characterization. The resultant LIGCs are characterized through SEM with a JEOL 6500F SEM at 5 kV with working distance of 10 mm. Raman spectra are collected with a Renishaw Raman microscope using a 514 nm laser with a power of 5 mW. XPS data are collected with a PHI Quantera SXM Scanning X-ray Microprobe with a base pressure of 5×10^{-9} Torr. Survey spectra are recorded using 0.5 eV step sizes with a pass energy of 140 eV. Elemental spectra are recorded using 0.1 eV step sizes with a pass energy of 26 eV. All of the XPS spectra are corrected using the C 1s peaks (284.5 eV) as reference.

Anti-Icing Procedure. The LIGC sample is attached on a glass slide with a thermocouple between sample and glass slide. The entire setup is placed at 45° to the horizontal plane in an insulated box cooled to −20 °C by dry ice. Water is added dropwise to the top of the LIGC to see if it freezes on the surface of the composite.

Deicing Procedure. The LIGC sample is attached to a glass slide with a thermocouple between the sample and glass slide. A piece of ice is frozen on the sample surface. The entire setup is placed at 45° to the horizontal plane in an insulated box cooled to −20 °C by dry ice. DC bias is applied at two electrodes on both ends of the sample treated with silver paint. After the power is switched on, the temperature change and time from start to ice sliding down from sample is recorded. The deicing voltages on LIGC−PC, −AAG, −LP,−PDMS, and −epoxy are 7.5 V cm^{-1} and on LIGC−PP, −PE, and −PS are 7.5, 10, and 15 V cm^{-1}, respectively.

Fabrication of a LIGC Resistive Memory. LIG in the LIGC−PDMS are made with 1000 PPI, 5% duty cycle. The 100 nm thick Al electrodes are deposited on the LIGC−PDMS by e-beam evaporation with a shadow mask (Figure S10f). Before the deposition of metal electrodes, the LIGC−PDMS is treated by oxygen plasma in order to modify the

DOI: 10.1021/acsnano.8b09626
ACS Nano XXXX, XXX, XXX−XXX

surface properties using reactive ion etching (RIE, O_2, 50 W, 20 sccm, 50 mTorr, 1−5 min). The memory device's performance is measured using a B1500A semiconductor device analyzer (Agilent Technologies).

Bacterial Culture. A mixed culture is prepared by adding 1 mL of secondary treated wastewater (aeration pond, Kibbutz Sde Boqer, Israel) to lysogeny broth (LB) (50 mL) and incubated at 30 °C. The cells are harvested in mid exponential phase and verified by measuring the optical density at 600 nm. The culture is centrifuged at 4000 rpm for 15 min and the cells are washed three times with 0.9% saline solution to remove residual medium constituents. The bacterial cells are diluted to ~10^8 colony-forming units (CFU) mL^{-1} in 0.9% saline solution and used for further experiments.

Biofilm Growth Experiments and Analysis. A mixed culture is grown in LB until the mid-exponential phase as above, and the cells are collected and washed with LB broth and further diluted to 0.1 OD at 600 nm in LB broth. A flow cell is used for biofilm growth experiments, previously reported in detail,[20,21] and in the same way, the LIG composites along with respective controls are tested. Briefly, samples are attached to a glass slide with epoxy glue and placed in the flow cell vertically. Inoculation of the mixed bacteria culture is performed by flowing 50 mL of the bacterial suspension (0.1 $OD_{600\ nm}$ in LB) through the flow cell at a rate of 2.5 mL min^{-1}. Then a sterile nutrient media (10% LB) is flowed at 2.0 mL min^{-1} through the flow cell for 36 h. CLSM (Zeiss LSM 510, META) is used for the biofilm evaluation, equipped with a Zeiss dry objective Plan-NeoFluar, as previously described. Live, dead, and EPS are evaluated after the samples are dyed with SYTO 9, propidium iodide, and concanavalin A (Con A) conjugated to Alexa Fluor 633 dye, respectively. Representative biofilm images are prepared by Imaris 3D imaging software (Bitplane, Zurich, Switzerland), and COMSTAT on Mathlab 2015b is used for quantitative analysis (biofilm volume and average thickness).

LIG Composite Antimicrobial Activity as an Electrode. Electrodes (7 cm^2) are fabricated on PDMS and PC as explained previously. Graphite wires are connected to the LIG electrodes by carbon-based glue, and further connections are protected with epoxy glue. The LIG composite electrodes are suspended in a beaker containing an aqueous solution of NaCl (150 mL, 0.05 M) with mix culture (~10^6 CFU mL^{-1}) of bacterial suspension. The power is adjusted to 0, 1.5, 2.0, or 2.5 V, and 150 μL samples are withdrawn from the reactor and used for CFU enumeration.

ASSOCIATED CONTENT

Supporting Information

The Supporting Information is available free of charge on the ACS Publications website at DOI: 10.1021/acsnano.8b09626.

LIGC with a porous surface that quickly wicks water droplets inside the composite (video S1) (AVI)

Deicing at ~ −40 °C with ice sliding off the surface after a DC bias was applied (video S2) (AVI)

Superhydrophobic surfaces of LIGCs prevent incoming droplets from freezing on the surface at −20 °C (video S3) (AVI)

Photos, graphs, schemes and SEM images (PDF)

AUTHOR INFORMATION

Corresponding Authors

*E-mail: arnusch@bgu.ac.il.

*E-mail: tour@rice.edu.

ORCID

Swatantra P. Singh: 0000-0003-1898-3378

Tuo Wang: 0000-0002-0990-3957

Christopher J. Arnusch: 0000-0002-1462-1081

James M. Tour: 0000-0002-8479-9328

Present Address

[&](S.P.S.) Center for Environmental Science and Engineering (CESE), Indian Institute of Technology Bombay, Powai, Mumbai 400076, India.

Author Contributions

[▽]D.X.L., K.Y., and J.Y. contributed equally to this work.

Notes

The authors declare the following competing financial interest(s): Rice University owns intellectual property rights to the LIG process and materials. Those rights are being licensed to a company in which J.M.T. might become a shareholder, though not an officer, director or employee. All potential conflicts of interest are managed through regular disclosure to and oversight by the Rice University Office of Sponsored Programs and Research Compliance.

ACKNOWLEDGMENTS

This work was funded by the Air Force Office of Scientific Research (FA9550-14-1-0111). We gratefully acknowledge the support of Universal Laser Systems for generously providing the XLS10MWH laser system with Multiwave Hybrid technology that was used for this research. The staff of Universal Laser Systems kindly provided regular helpful advice. The use of the thermal heating therapy in this work did not meet the definition of human subject research at Rice University; therefore, no IRB protocol approval was needed. We are grateful to the United States−Israel Binational Science Foundation (BSF Grant No. 2014233) for financial support for the experiments performed at BGU. C.J.A. thanks the Canadian Associates of Ben Gurion University (CABGU) Quebec region for support.

REFERENCES

(1) Castro Neto, A. H.; Guinea, F.; Peres, N. M. R.; Novoselov, K. S.; Geim, A. K. The Electronic Properties of Graphene. *Rev. Mod. Phys.* **2009**, *81*, 109−162.

(2) Lee, C.; Wei, X.; Kysar, J. W.; Hone, J. Measurement of the Elastic Properties and Intrinsic Strength of Monolayer Graphene. *Science* **2008**, *321*, 385−388.

(3) Balandin, A. A.; Ghosh, S.; Bao, W.; Calizo, I.; Teweldebrhan, D.; Miao, F.; Lau, C. N. Superior Thermal Conductivity of Single-Layer Graphene. *Nano Lett.* **2008**, *8*, 902−907.

(4) Geim, A. K.; Novoselov, K. S. The Rise of Graphene. *Nat. Mater.* **2007**, *6*, 183.

(5) Novoselov, K. S.; Geim, A. K.; Morozov, S. V.; Jiang, D.; Zhang, Y.; Dubonos, S. V.; Grigorieva, I. V.; Firsov, A. A. Electric Field Effect in Atomically Thin Carbon Films. *Science* **2004**, *306*, 666−669.

(6) Allen, M. J.; Tung, V. C.; Kaner, R. B. Honeycomb Carbon: a Review of Graphene. *Chem. Rev.* **2010**, *110*, 132−145.

(7) Chyan, Y.; Ye, R.; Li, Y.; Singh, S. P.; Arnusch, C. J.; Tour, J. M. Laser-Induced Graphene by Multiple Lasing: Toward Electronics on Cloth, Paper, and Food. *ACS Nano* **2018**, *12*, 2176−2183.

(8) Ye, R.; Chyan, Y.; Zhang, J.; Li, Y.; Han, X.; Kittrell, C.; Tour, J. M. Laser-induced Graphene Formation on Wood. *Adv. Mater.* **2017**, *29*, 1702211.

(9) Lin, J.; Peng, Z.; Liu, Y.; Ruiz-Zepeda, F.; Ye, R.; Samuel, E. L. G.; Yacaman, M. J.; Yakobson, B. I.; Tour, J. M. Laser-Induced Porous Graphene Films from Commercial Polymers. *Nat. Commun.* **2014**, *5*, 5714.

(10) Luong, D. X.; Subramanian, A. K.; Silva, G. A. L.; Yoon, J.; Cofer, S.; Yang, K.; Owuor, P. S.; Wang, T.; Wang, Z.; Lou, J.; Ajayan, P. M.; Tour, J. M. Laminated Object Manufacturing of 3D-Printed Laser-Induced Graphene Foams. *Adv. Mater.* **2018**, *30*, 1707416.

(11) Deng, H.; Zhang, C.; Su, J.-W.; Xie, Y.; Zhang, C.; Lin, J. Bioinspired Multi-Responsive Soft Actuators Controlled by Laser Tailored Graphene Structures. *J. Mater. Chem. B* **2018**, *6*, 5415−5423.

DOI: 10.1021/acsnano.8b09626
ACS Nano XXXX, XXX, XXX−XXX

(12) Zhang, C.; Xie, Y.; Deng, H.; Tumlin, T.; Zhang, C.; Su, J. W.; Yu, P.; Lin, J. Monolithic and Flexible ZnS/SnO_2 Ultraviolet Photodetectors with Lateral Graphene Electrodes. *Small* **2017**, *13*, 1604197.
(13) Ye, R.; James, D. K.; Tour, J. M. Laser-Induced Graphene. *Acc. Chem. Res.* **2018**, *51*, 1609−1620.
(14) Duy, L. X.; Peng, Z.; Li, Y.; Zhang, J.; Ji, Y.; Tour, J. M. Laser-Induced Graphene Fibers. *Carbon* **2018**, *126*, 472−479.
(15) Li, Y.; Luong, D. X.; Zhang, J.; Tarkunde, Y. R.; Kittrell, C.; Sargunaraj, F.; Ji, Y.; Arnusch, C. J.; Tour, J. M. Laser-Induced Graphene in Controlled Atmospheres: From Superhydrophilic to Superhydrophobic Surfaces. *Adv. Mater.* **2017**, *29*, 1700496.
(16) Zhang, J.; Ren, M.; Li, Y.; Tour, J. M. *In Situ* Synthesis of Efficient Water Oxidation Catalysts in laser-Induced Graphene. *ACS Energy Lett.* **2018**, *3*, 677−683.
(17) Smith, M. K.; Luong, D. X.; Bougher, T. L.; Kalaitzidou, K.; Tour, J. M.; Cola, B. A. Thermal Conductivity Enhancement of Laser Induced Graphene Foam upon P3HT Infiltration. *Appl. Phys. Lett.* **2016**, *109*, 253107.
(18) Li, L.; Zhang, J.; Peng, Z.; Li, Y.; Gao, C.; Ji, Y.; Ye, R.; Kim, N. D.; Zhong, Q.; Yang, Y.; Fei, H.; Ruan, G.; Tour, J. M. High-Performance Pseudocapacitive Microsupercapacitors from laser-Induced Graphene. *Adv. Mater.* **2016**, *28*, 838−845.
(19) Ye, R.; Peng, Z.; Wang, T.; Xu, Y.; Zhang, J.; Li, Y.; Nilewski, L. G.; Lin, J.; Tour, J. M. *In Situ* Formation of Metal Oxide Nanocrystals Embedded in Laser-Induced Graphene. *ACS Nano* **2015**, *9*, 9244−9251.
(20) Singh, S. P.; Li, Y.; Zhang, J.; Tour, J. M.; Arnusch, C. J. Sulfur-Doped Laser-Induced Porous Graphene Derived from Polysulfone-Class Polymers and Membranes. *ACS Nano* **2018**, *12*, 289−297.
(21) Singh, S. P.; Li, Y.; Be'er, A.; Oren, Y.; Tour, J. M.; Arnusch, C. J. Laser-Induced Graphene Layers and Electrodes Prevents Microbial Fouling and Exerts Antimicrobial Action. *ACS Appl. Mater. Interfaces* **2017**, *9*, 18238−18247.
(22) Ye, R.; James, D. K.; Tour, J. M. Laser-Induced Graphene: from Discovery to Translation. *Adv. Mater.* **2019**, *31*, 1803621.
(23) Singh, S. P.; Ramanan, S.; Kaufman, Y.; Arnusch, C. J. Laser-Induced Graphene Biofilm Inhibition: Texture Does Matter. *ACS Appl. Nano Mater.* **2018**, *1*, 1713−1720.
(24) Rahimi, R.; Ochoa, M.; Yu, W.; Ziaie, B. Highly Stretchable and Sensitive Unidirectional Strain Sensor *via* Laser Carbonization. *ACS Appl. Mater. Interfaces* **2015**, *7*, 4463−4470.
(25) Wu, Y.; Karakurt, I.; Beker, L.; Kubota, Y.; Xu, R.; Ho, K. Y.; Zhao, S.; Zhong, J.; Zhang, M.; Wang, X.; Lin, L. Piezoresistive Stretchable Strain Sensors with Human Machine Interface Demonstrations. *Sens. Actuators, A* **2018**, *279*, 46−52.
(26) Song, W.; Zhu, J.; Gan, B.; Zhao, S.; Wang, H.; Li, C.; Wang, J. Flexible, Stretchable, and Transparent Planar Microsupercapacitors Based on 3D Porous Laser-Induced Graphene. *Small* **2018**, *14*, 1702249.
(27) Sun, B.; McCay, R. N.; Goswami, S.; Xu, Y.; Zhang, C.; Ling, Y.; Lin, J.; Yan, Z. Gas-Permeable, Multifunctional On-Skin Electronics Based on Laser-Induced Porous Graphene and Sugar-Templated Elastomer Sponges. *Adv. Mater.* **2018**, *30*, 1804327.
(28) Ferrari, A. C. Raman Spectroscopy of Graphene and Graphite: Disorder, Electron−Phonon Coupling, Doping and Nonadiabatic Effects. *Solid State Commun.* **2007**, *143*, 47−57.
(29) Whyman, G.; Bormashenko, E.; Stein, T. The Rigorous Derivation of Young, Cassie−Baxter and Wenzel Equations and the Analysis of the contact Angle Hysteresis Phenomenon. *Chem. Phys. Lett.* **2008**, *450*, 355−359.
(30) Cassie, A.; Baxter, S. Wettability of Porous Surfaces. *Trans. Faraday Soc.* **1944**, *40*, 546−551.
(31) Li, Z.; Xu, Z.; Liu, Y.; Wang, R.; Gao, C. Multifunctional Non-Woven Fabrics of Interfused Graphene Fibres. *Nat. Commun.* **2016**, *7*, 13684.
(32) Ge, J.; Shi, L.-A.; Wang, Y.-C.; Zhao, H.-Y.; Yao, H.-B.; Zhu, Y.-B.; Zhang, Y.; Zhu, H.-W.; Wu, H.-A.; Yu, S.-H. Joule-Heated Graphene-Wrapped Sponge Enables Fast Clean-Up of Viscous Crude-Oil Spill. *Nat. Nanotechnol.* **2017**, *12*, 434.
(33) Kang, J.; Kim, H.; Kim, K. S.; Lee, S.-K.; Bae, S.; Ahn, J.-H.; Kim, Y.-J.; Choi, J.-B.; Hong, B. H. High-Performance Graphene-Based Transparent Flexible Heaters. *Nano Lett.* **2011**, *11*, 5154−5158.
(34) Zhou, R.; Li, P.; Fan, Z.; Du, D.; Ouyang, J. Stretchable Heaters with Composites of an Intrinsically Conductive Polymer, Reduced Graphene Oxide and an Elastomer for Wearable Thermotherapy. *J. Mater. Chem. C* **2017**, *5*, 1544−1551.
(35) Michlovitz, S.; Hun, L.; Erasala, G. N.; Hengehold, D. A.; Weingand, K. W. Continuous Low-Level Heat Wrap Therapy is Effective for Treating Wrist Pain. *Arch. Phys. Med. Rehabil.* **2004**, *85*, 1409−1416.
(36) Yang, J. J.; Strukov, D. B.; Stewart, D. R. Memristive Devices for Computing. *Nat. Nanotechnol.* **2013**, *8*, 13.
(37) Pan, F.; Gao, S.; Chen, C.; Song, C.; Zeng, F. Recent Progress in Resistive Random Access Memories: Materials, Switching Mechanisms, and Performance. *Mater. Sci. Eng., R* **2014**, *83*, 1−59.
(38) Jo, A.; Seo, Y.; Ko, M.; Kim, C.; Kim, H.; Nam, S.; Choi, H.; Hwang, C. S.; Lee, M. J. Textile Resistance Switching Memory for Fabric Electronics. *Adv. Funct. Mater.* **2017**, *27*, 1605593.
(39) Evertsson, J.; Bertram, F.; Zhang, F.; Rullik, L.; Merte, L.; Shipilin, M.; Soldemo, M.; Ahmadi, S.; Vinogradov, N.; Carlà, F. The Thickness of Native Oxides on Aluminum Alloys and Single Crystals. *Appl. Surf. Sci.* **2015**, *349*, 826−832.

DOI: 10.1021/acsnano.8b09626
ACS Nano XXXX, XXX, XXX−XXX